

X-ray Photoelectron Spectroscopy and Resonant X-ray Spectroscopy Investigations of Interactions between Thin Metal Catalyst Films and Amorphous Titanium Dioxide Photoelectrode Protection Layers

Matthias H. Richter,[‡] Wen-Hui Cheng,[‡] Ethan J. Crumlin, Walter S. Drisdell, Harry A. Atwater, Dieter Schmeißer, Nathan S. Lewis,^{*} and Bruce S. Brunschwig^{*}



Cite This: *Chem. Mater.* 2021, 33, 1265–1275



Read Online

ACCESS |



Metrics & More

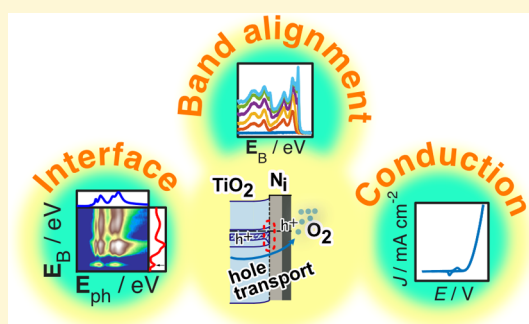


Article Recommendations



Supporting Information

ABSTRACT: The use of electrochemistry, X-ray photoelectron spectroscopy, and resonant X-ray spectroscopy has unlocked the paradox of interfacial hole conduction through amorphous TiO₂ (a-TiO₂) to deposited Ni, Ir, and Au metal catalysts. Although electrocatalysts for the oxygen-evolution reaction derived from metallic Ir and Ni have mutually similar overpotentials in alkaline media, Si/a-TiO₂/Ir interfaces exhibit higher overpotentials than Si/a-TiO₂/Ni interfaces. The data allow formulation of full band energy diagrams for n-Si/a-TiO₂/metal interfaces for M = Ni, Ir, or Au. Although both Ni and Ir produce band bending in a-TiO₂ favoring hole conduction, only Ni creates multiple states within the a-TiO₂ band gap at the a-TiO₂/Ni interface, which produces a quasi-metallic interface at the a-TiO₂/Ni junction. Au, however, produces a flat-band interface that limits hole conduction without any new band gap states.



1. INTRODUCTION

Dual-junction light absorbers with tailored band gaps, typically formed from silicon and/or III–V semiconductors, can potentially provide high efficiencies in integrated photoelectrochemical (PEC) water-splitting devices.^{1,2} Analogous systems incorporating triple-junction light absorbers selectively produce reduced carbonaceous products by CO₂ reduction.^{3–5} However, the photoactive components in Si or III–V photoelectrodes are typically unstable in aqueous media and either corrode or form a nonconductive passivation layer unless protected by transparent, conducting, chemically robust protective layers.^{6–8} Amorphous TiO₂ (a-TiO₂) coatings are stable in highly alkaline solutions and can transfer charge from the semiconductor to suitable catalysts. These films can act as protection layers and antireflection coatings on PEC electrodes. Notably, a-TiO₂ coatings deposited at low temperatures (<300 °C) by atomic-layer deposition (ALD) using tetrakis(dimethylamino)titanium(IV) (TDMAT) yield protected photoanodes that allow for facile interfacial hole transport.⁶

Hole conduction in such systems has been proposed to occur in the presence of a “defect” band within the band gap of the TDMAT a-TiO₂ protection layer.^{6,9,10} The activation energy for conduction decreases with decreasing temperature, indicating that neither the valence nor conduction bands are the primary pathway for hole conduction.⁹ The data are moreover consistent with a hopping mechanism between Ti⁴⁺ and Ti³⁺ sites. The conductivity and intensity of the gap state emission detected by X-ray photoelectron spectroscopy (XPS)

correlate with the concentration of Ti³⁺ sites in the a-TiO₂ films.

The conductivity of a-TiO₂ films is dependent on the nature of the metal contact. Bare a-TiO₂ deposited on a p⁺-Si electrode produces a rectifying a-TiO₂/liquid interface. The a-TiO₂ has a high overpotential and is a kinetically slow catalyst for water oxidation.^{6,9,10} However, when coated with an appropriate metal catalyst, such as Ni, a-TiO₂-protected photoanodes exhibit high catalytic exchange-current densities and low overpotentials for water oxidation. Metals with greater work-functions than a-TiO₂ generally produce lower conductivities across the a-TiO₂/metal interface than metals with low work-functions. This behavior is consistent with the hypothesis that high work-function metals deplete the Ti³⁺ hopping sites near the TiO₂ surface and block hopping-based conduction at the surface.⁹ Low work-function metals are normally expected to produce ohmic contacts to a-TiO₂ and not deplete Ti³⁺ sites.¹¹ However, Ni, a high work-function metal, exhibits interfacial conductivity with a-TiO₂ that is comparable to that obtained by the use of metals with low

Received: October 15, 2020

Revised: January 25, 2021

Published: February 11, 2021



work-functions. Hence, properties other than the work-function must contribute to the differences in interfacial conductivity.⁹ Under oxidative conditions in alkaline media, the top surface of a Ni contact converts to NiO_x, an active catalyst for water oxidation. Thus, Ni is the preferred material for contacting a-TiO₂ for use as a photoanode for water oxidation.⁹

The operation of a photoanode depends on multiple properties such as the optical transmission of the catalyst,⁷ the activity of the catalyst,¹² changes in the catalyst activity with thickness,^{13–15} and interfacial effects between the semiconductor and the protection layer.^{16,17} Direct conduction comparisons between TiO₂ and metal catalysts for water oxidation have been performed, and they show the superiority of the Ni coatings compared to Pt, Pd, Ir, Au, Mg, and Ti films.⁹

Deposition of ultrathin metal films or nanoparticles on oxide surfaces exhibits unique properties for catalytic systems.¹⁸ Deposition of thin Cr metal films on rutile TiO₂,¹⁹ treatment of TiO₂ with hydrogen^{20–22} or K,²³ and doping of TiO₂ with nitrogen²⁴ all result in the appearance of an XPS emission band within the band gap of TiO₂. The Ti in a-TiO₂ has a distorted octahedral symmetry (O_h) with a valence configuration of O 2p⁶ and Ti [Ar]3d⁰4s⁰, resulting in a relatively “pure” O 2p valence band (VB) and Ti 3d/4s conduction band (CB).²⁵ The six oxygen ligands break the Ti 3d orbitals into lower-energy states of t_{2g} symmetry and higher-energy states of e_g symmetry.²⁵ Oxygen vacancies in TiO₂ result in n-type doping of the crystal and produce Ti³⁺ sites.²⁵

The nature of the defect states that reside in the band gap of TiO₂ has been extensively studied.^{26–28,22} States in the band gap have been observed for both crystalline and amorphous TiO₂ films. The surficial defects can be engineered to enhance or remove these states.^{29,30} The defects in the bulk have primarily been ascribed to Ti in special sites, with resonant photoemission spectroscopy suggesting that the states are associated with the Ti³⁺ centers.^{31,32} Theoretical calculations suggest that oxygen vacancies can lead to both six- and five-coordinated Ti³⁺ sites as well as six-coordinated Ti³⁺–OH sites and Ti³⁺ interstitials.^{22,27} Most of the experimental results indicate the presence of oxygen vacancies, with recent works suggesting that interstitial Ti³⁺ sites in the near-surface region provide a major contribution to the gap state.^{27,26} Usually, the gap state in the bulk of a-TiO₂ is assigned to Ti³⁺ sites that have a partially populated band derived from t_{2g} orbitals, which are formally unoccupied due to the d⁰ character of TiO₂.³³

To understand the differences in conduction between Ni, Ir, and Au contacts, resonant photoemission spectroscopy (resPES) and resonant inelastic X-ray scattering (RIXS) measurements at the Ti 2p edge have been used here to investigate the a-TiO₂ gap state at buried a-TiO₂/metal interfaces. After X-ray excitation of a Ti 2p core-level electron into an e_g CB state, de-excitation from a t_{2g} VB state into the core-level hole creates an intermediate state with an electron and a hole in e_g and t_{2g} bands, respectively (i.e., a d–d transition). By our use of resonance X-ray spectroscopy, the ground state is excited to an initial CB excited state that decays either by emission of an Auger electron (resPES) or to a second state by emission of an X-ray (RIXS) (Figure S1). The lifetime of the CB excited state defines the absorption bandwidth. The lifetime of the second state with a VB hole defines the width of the VB resonances.³⁴ Resonant X-ray spectroscopy is a two-dimensional technique, with resPES and

RIXS using excitation energies and either the photoelectron or difference between the excitation and emitted X-ray energies, respectively. Thus, the X-ray absorption spectrum (XAS) is split into individual resPES or RIXS regions.

The cross section for resonant excitation (e.g., from a core to the CB level) of an element is orders of magnitude larger than that for elements not in resonance. The increased absorption cross section and the decay processes of the resonantly created core hole allow the determination of the contribution of that element to the total density of states of the compound. Hence, resPES and RIXS can provide the contribution of a particular element to the full density of states. For resPES or RIXS VB spectra, the excitation energy is scanned through the core-level absorption energies of the elements of interest while either the emitted electrons or X-rays are analyzed. By monitoring the total absorption as the excitation energy is scanned, an XAS spectrum can also be collected, enabling elucidation of the CB states.

2. EXPERIMENTAL SECTION

Films of a-TiO₂ prepared by ALD^{6,35–37} were deposited on degenerately doped (resistivity $\rho < 0.005 \Omega\text{-cm}$) p⁺-type Si substrates. The Si(100) wafers were first cleaned via an oxidizing etch by soaking for 2 min in a “piranha” solution consisting of a 3:1 ratio (by volume) of concentrated H₂SO₄ (98%) to 30% H₂O₂ (aq) followed by 10 s in a 10% (by volume) solution of HF (aq). The wafers were then immediately etched for 10 min at 75 °C in a 5:1:1 (volume ratio) solution of H₂O, 36% HCl (aq), and 30% H₂O₂ (aq) before being moved into the ALD chamber. The a-TiO₂ was deposited in a Cambridge Nanotech Savannah ALD reactor using tetrakis-(dimethylamino)titanium (TDMAT) as the precursor. During deposition, the sample was kept at 150 °C, TDMAT was at 75 °C, H₂O was at room temperature, and the background pressure was 0.22 Torr. A cycle consisted of a 0.1 s pulse of TDMAT, then a 15 s purge of N₂ at 20 sccm, followed by a 0.015 s pulse of H₂O, and a final 15 s purge with N₂. This process was repeated for 1500 cycles to reach ~70 nm in thickness. Metals were deposited using an electron beam evaporator (System 02520, Angstrom Engineering) with a base pressure of 1×10^{-7} Torr at a rate of 0.1 to 1 Å·s⁻¹. As appropriate, Ni was deposited at a RF sputtering power of 150 W for 20–300 s using an AJA International sputtering system at a rate of ~2 nm·min⁻¹. Samples were then exposed to the atmosphere.

Resonant XPS experiments were performed at the soft X-ray beamline U49/2-PGM2 at BESSY II in Berlin.³⁸ The photon energy resolution was ~30 meV. All spectra were corrected for the incoming photon flux. For resPES VB spectra at the Ti 2p, O 1s, and Ni 2p edges, the photon excitation energy was varied over a wide range (452–475 eV; 525–550 eV; and 845–865 eV, respectively) by sweeping the undulator gap and the monochromator in parallel. The electron analyzer was a SPECS Phoibos 150 with a 1D delay line electron detector, and the resolution of the spectrometer was 70 meV. The resolution was 30 meV for XAS (CB) measurements and ~80 meV for PES (VB). To compensate for the polarization dependence of the resonances, samples were positioned at a magic incidence angle of 54.7°. ³⁹ For the Ti 2p, O 1s, and Ni 2p edges, the photon energy step size was 0.20 eV with a binding energy step size of 0.40 eV, resulting in a total of 115, 125, and 100 VB spectra, respectively.

For select excitation energies, additional resonant XPS experiments were performed at the Advanced Light Source, Berkeley at beamline 9.3.2 using the soft X-ray ambient-pressure XPS end station equipped with a VG-Scienta R4000 HiPP analyzer.⁴⁰ RIXS experiments were performed at the Advanced Light Source, Berkeley at beamline 8.0.1 using the iRIXS end station equipped with two slitless variable line-spacing (VLS) grating spectrographs with a resolution of ~0.3 eV.⁴¹ XAS data were collected in the total electron yield (TEY) mode and in the total fluorescence yield mode. All data were normalized by the incident X-ray flux as measured by a Au mesh positioned upstream of

the sample. Energies were calibrated using the XAS of TiO₂ as a reference.

Laboratory XPS measurements were performed using a Kratos Axis Ultra system with a base pressure of $<1 \times 10^{-9}$ Torr. A monochromatic Al K α (1486.69 eV) source with a power of 150 W was used for all measurements. For ultraviolet photoelectron spectroscopy (UPS), a He gas discharge lamp provided He I excitation (21.21 eV) for measurement of the work-function of the sample. A minimum of six samples was measured for work-function data. Prior to UPS measurements, pure metal samples (99.99%) were sputter-cleaned until no contamination or carbon was detectable. Freshly prepared samples were transferred from the ALD to the XPS/UPS system under a nitrogen atmosphere using a portable XPS transfer suitcase. No sputter cleaning was performed because tests showed that oxygen was preferentially sputtered.

Electrochemical characterization was performed in a three-electrode configuration using a Biologic SP-200 potentiostat with a Ag/AgCl reference electrode and a carbon counter electrode. To assess the conductivity of the samples, a vigorously stirred solution containing 0.05 M Fe(CN)₆³⁻ and 0.35 M Fe(CN)₆⁴⁻ was used as the electrolyte. Oxygen-evolution reaction (OER) measurements were conducted in 1.0 M KOH (aq).

X-ray diffraction (XRD) data were collected using a Bruker Discover D8 XRD with a microfocus X-ray source (Cu) and a VANTEC-500 large microgap detector. Scanning electron microscopy (SEM) images were obtained with an FEI Nova NanoSEM 450 microscope.

3. RESULTS

3.1. Electrochemical Performance and Surface Structure. The current density versus potential (J - E) behavior in 1.0 M KOH (aq) for p⁺-Si/a-TiO₂/Ni (20 nm) and p⁺-Si/a-TiO₂/Ir (20 nm) contacts is shown in Figure 1a. Peaks at $E = +1.44$ V and +1.35 V versus RHE, corresponding to Ni(II)/Ni(III) oxidations and reductions, respectively, were observed

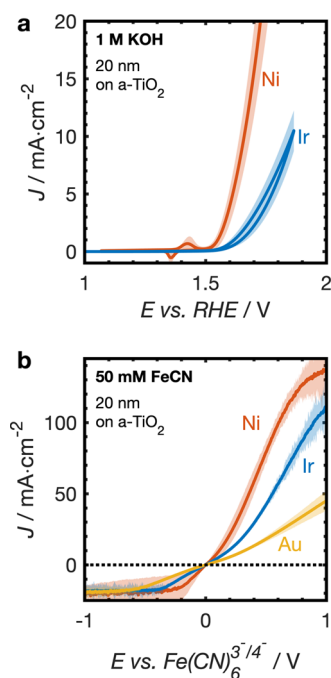


Figure 1. J - E measurements for p⁺-Si/a-TiO₂/M. (a) M = Ni and Ir in 1.0 M KOH (aq). (b) M = Ni, Ir, and Au in contact with 0.05 M Fe(CN)₆³⁻ and 0.35 M Fe(CN)₆⁴⁻ (aq). The solid lines represent an average over five samples, and the standard deviation is shown as the shaded area.

prior to the onset of the OER for the p⁺-Si/a-TiO₂/Ni sample. Ir and Ni metals have mutually similar overpotentials for the OER in alkaline media.¹² Although pure Ni exhibits high overpotentials ($\eta_{10\text{mA}/\text{cm}^2} = 700$ mV) in KOH solution under anodic conditions, Ni oxidizes to NiO_x and extracts Fe from the KOH solution. The NiFe catalysts show overpotentials as low as $\eta_{10\text{mA}/\text{cm}^2} = 350$ mV.^{42,12} The difference between the best NiFe and Ir catalysts is only 50 mV. However, at a current density of 10 mA cm⁻², the overpotential for p⁺-Si/a-TiO₂/Ir (20 nm) was ~250 mV larger than that of p⁺-Si/a-TiO₂/Ni (20 nm) (Figure 1a). Moreover, in contact with a reversible one-electron redox couple, Fe(CN)₆^{3-/4-}, the interfacial charge-transfer kinetics decreased in the order p⁺-Si/a-TiO₂/Ni (20 nm) > p⁺-Si/a-TiO₂/Ir (20 nm) > p⁺-Si/a-TiO₂/Au (20 nm) (Figure 1b).

The trend in the interfacial kinetics of Ni > Ir > Au does not correlate with that of the work-function or metal nobility because the work-functions decrease in the order Ir > Au \approx Ni^{43,44} Figure S2 shows that a Ni thickness of >2 nm was required to produce substantial interfacial conductivity, with ultrathin layers exhibiting essentially no conductivity. For Ir, interfacial conductivity was observed for a metal thickness of ≥ 0.5 nm, with the conductivity increasing with thickness, saturating after deposition of ~10 nm of Ir. Hole conduction for a-TiO₂/Au was observed only for Au ≥ 10 nm.

Ni and Ir layers on a-TiO₂ formed a smooth surface film that showed no distinctive surface features by SEM (Figure S3). However, for a-TiO₂/Au, at a thickness of ≤ 5 nm, the Au layer was composed of nanoparticles that began to interconnect with deposition of more Au at a thickness of ~10 nm. The particle size distribution for a-TiO₂/Au (5 nm) indicates an average particle diameter of 20 nm with a gap size of <20 nm (Figure S4a). Figure S5 shows XRD spectra of samples of TDMAT a-TiO₂ with metal contacts ranging from 0.01 to 30 nm in thickness. The (111) metal diffraction peak became more pronounced as the metal layer thickness increased, with additional (200), (220), and (311) peaks observed for Au. No XRD signal from TDMAT a-TiO₂ was observed on any of the samples.

3.2. Surface Chemistry and Energetics. High-resolution XPS data as a function of metal thickness for a-TiO₂/M interfaces for Ni 2p, Ir 4f, Au 4f, Ti 2p, and O 1s core levels and for the VB region are shown in Figure 2. The VB spectra of bare a-TiO₂ showed the characteristic gap state at ~1 eV binding energy (BE), as shown in Figure 2d,h,l and Figure S6c.

The surface sensitivity of the gap state was measured by angle-resolved XPS, and the signal intensity did not change for photoelectron emission angles between 0 and 70° off-normal incidence, giving no evidence of a change of the gap state at the surface (Figure S6). The gap state was also observed by RIXS, which probes deeper into the TiO₂ because the X-ray attenuation length is substantially longer than the photoelectron escape depth, as shown in Figure S7. Measurements on a sample stored for over a year in air showed essentially no change in the gap state, as shown in Figure S7.

For Ni layers with a thickness >0.1 nm, the intensity of the Ni VB states prevented the observation of the a-TiO₂ gap state with laboratory XPS instrumentation (Figure 2d). Samples with Ni or Ir layers showed metal oxide peaks (Figure 2a,e) whose intensity relative to the metal peaks decreased as the thickness of the deposited metal increased. For Ni samples, increases in the thickness of the metal did not obscure the metal oxide peaks, indicating that the oxide was on the metal

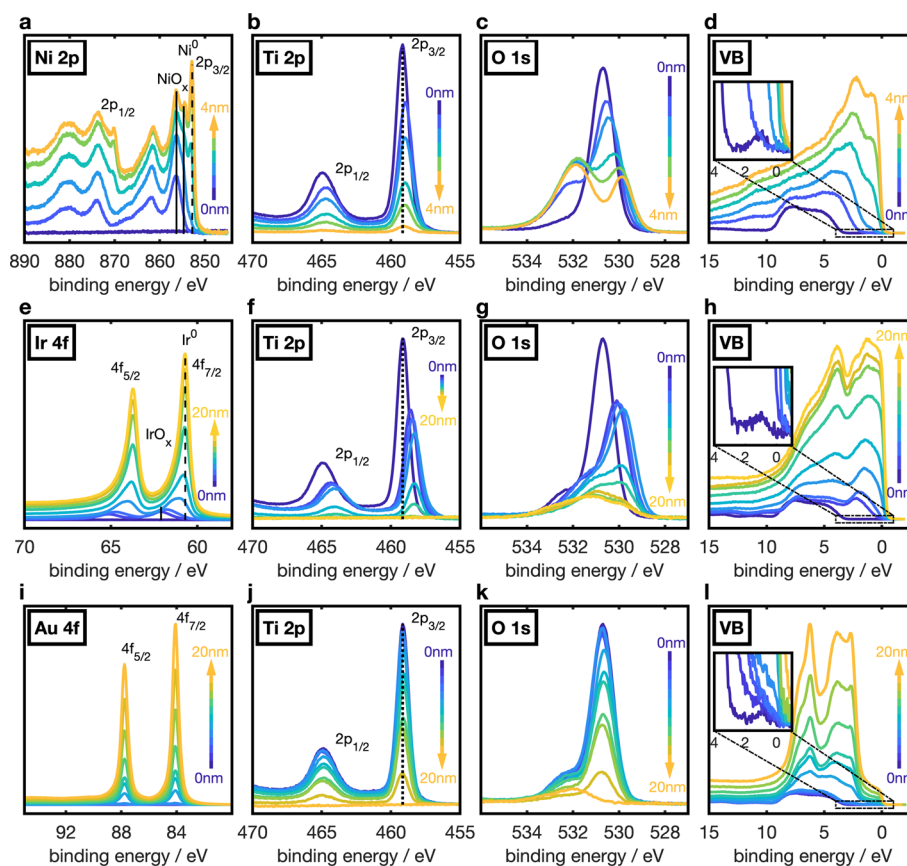


Figure 2. XPS data for a-TiO₂/metal systems for Ni (a–d), Ir (e–h), and Au (i–l) showing core-level peaks for the metal, Ni 2p (a), Ir 4f (e), Au 4f (i), Ti 2p (b, f, j), O 1s, (c, g, k), and VB (d, h, l). The metal overlayer thicknesses are shown in the graph. The black dotted line shown in the Ti 2p core-level plots indicates the position of bulk Ti 2p_{3/2} core-level peaks, whereas the dashed and solid lines in (a) and (e) indicate metallic and oxide peak positions, respectively.

surface and not at the a-TiO₂ interface. Synchrotron XPS depth profiling performed by changing the excitation energy, and thus the inelastic mean free path (IMFP) of the emitted electrons, revealed that the NiO_x VB peak increased in intensity as the surface sensitivity increased. For ultrathin Ni layers of 0.3 nm thickness, XPS showed only NiO_x with no Ni metal (Figure S8b). In contrast, for thicker metallic layers, Ni⁰ states were observed at the Fermi energy (E_F) (Figure S8). Ambient-pressure XPS measurements indicated a metallic Ni phase for samples under an applied potential in 1 M KOH (aq).⁴⁵ No core-level shift was observed for the metal peaks (Ni 2p, Ir 4f, and Au 4f) (only changes in oxidation state), but BE shifts were observed for the Ti 2p core level for a-TiO₂/Ni and a-TiO₂/Ir samples.

No shoulder or change in peak shape (FWHM) was evident for the Ti 2p core level, indicating that the oxidation state of a-TiO₂ did not change, that is, no chemical transition was detected from Ti⁴⁺ to Ti³⁺ or lower oxidation states. Thus, the single component for the Ti 2p_{3/2} and Ti 2p_{1/2} core levels was assigned to Ti⁴⁺ and the shifts in the Ti 2p peak position were assigned to band bending in TiO₂ but not to a change of oxidation state.

Work-functions (Φ) were determined by UPS for a-TiO₂ and Ni, Ir, and Au (Figure 3a). The values were $\Phi_{\text{a-TiO}_2} = 4.7 \pm 0.10$ eV, $\Phi_{\text{Au}} = 5.05 \pm 0.22$ eV, $\Phi_{\text{Ni}} = 5.09 \pm 0.19$ eV, and $\Phi_{\text{Ir}} = 5.32 \pm 0.12$ eV, in good agreement with other experimental studies.^{46,43,44} The VB maximum (VBM) for TDMAT a-TiO₂ was observed at 2.94 ± 0.10 eV BE. The

ionization potentials (IP) for different phases and surface orientations of crystalline TiO₂ were measured as 7.4 and 7.9 eV for rutile and anatase, respectively.⁴⁷ Using a VBM BE of 2.94 eV gives work-functions of 4.5 and 5.0 eV, respectively, that bracket the value measured for a-TiO₂.

The band bending of a-TiO₂ obtained from the changes in the Ti 2p_{3/2} peak position shown in Figure 3c follows the trend of the difference in work-function between a-TiO₂ and the metal, $\Delta\Phi$. Differences between the magnitude of the band bending and $\Delta\Phi$ can be attributed to the interface dipole and Fermi level pinning (vide supra).

3.3. Interface Energetics and Chemistry. ResPES and RIXS measurements were used to investigate the buried a-TiO₂/metal interface. These techniques can examine the interface through the relatively thick metal layer and can measure the VB states of a-TiO₂ using resonant excitation of a particular element. Figure 4 shows a color contour plot for resPES VB spectra at the Ti L_{3,2} absorption edge for p⁺-Si/a-TiO₂/Ni (for details, see Supporting Information). The abscissa indicates the X-ray excitation energy (452 to 475 eV) and the ordinate shows the BE of the initially formed excited valence state (0 to 20 eV). To obtain only the resonant contributions to the VB, an off-resonant pre-edge reference VB spectrum (452 eV for the Ti L_{3,2} edge, 525 eV for O K edge, and 845 eV for Ni L₃ edge) was subtracted from all spectra at the corresponding edge, for example, to set the intensity to zero at the start of the scan.³⁹ Figure 4a shows the resPES data for p⁺-Si/a-TiO₂. The resPES probes the properties of the top

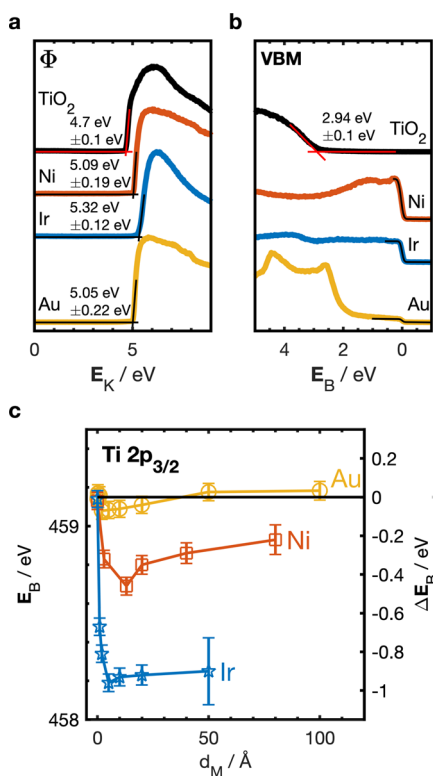


Figure 3. He I ultraviolet photoelectron spectra of TDMAT a-TiO₂/metal, with nickel, iridium, and gold showing the work-function (a) and VBM (b). The metals were sputter-cleaned until no contamination or carbon was detected. (c) Energy position of the Ti $2p_{3/2}$ core level depending on the contact metal and metal thickness. The values were extracted from Figure 2.

surface of a-TiO₂. In the resPES map, the characteristic gap state is clearly evident at a BE of 1 eV for both the L₃ (459.6 eV photon energy) and L₂ edges (465.2 eV photon energy) as well as in the VB spectrum shown in the right-hand side panel, indicated by an arrow. After deposition of 0.3 nm of Ni, no gap state was observed in the resPES map, as shown in Figure 4b. When the nickel thickness was 1.3 nm, two gap states were observed at 0.7 and 2.6 eV BEs, as shown in the right-hand side panel of Figure 4c. For this sample (p⁺-Si/a-TiO₂/Ni (1.3 nm)), the VB spectrum on the right axis was measured with an increased dwell time to improve the signal-to-noise ratio.

The resPES maps for the oxygen K and Ni L₃ edges are shown in Figures S9,S10. For 0.3 nm of Ni coverage, no oxygen VB states were observed between binding energies of 5–10 eV and photon energies between 530 and 535 eV (Figure S9a,b), in contrast to the observations for pristine a-TiO₂. With increased Ni thickness, oxygen states were, however, again observed in this BE region (Figure S9c). Oxygen signals arise from both NiO_x and a-TiO₂; thus, the states shown in Figure S9c,a may not originate from the same species. For Ni layers <0.3 nm thick, the Ni was completely oxidized (Figure 2a); however, for thicker layers, the Ni was oxidized only on the top surface and was metallic toward the a-TiO₂ surface. Due to the shielding of overlayers and elemental sensitivity, oxygen peaks observed for thicker layers by resPES are associated primarily with NiO_x rather than a-TiO₂. The corresponding Ni L₃ edge maps are shown in Figure S10. The two prominent features at photon energies of 853 and 854.7 eV can be attributed to Ni²⁺ (NiO) and Ni³⁺ (NiOOH) states,

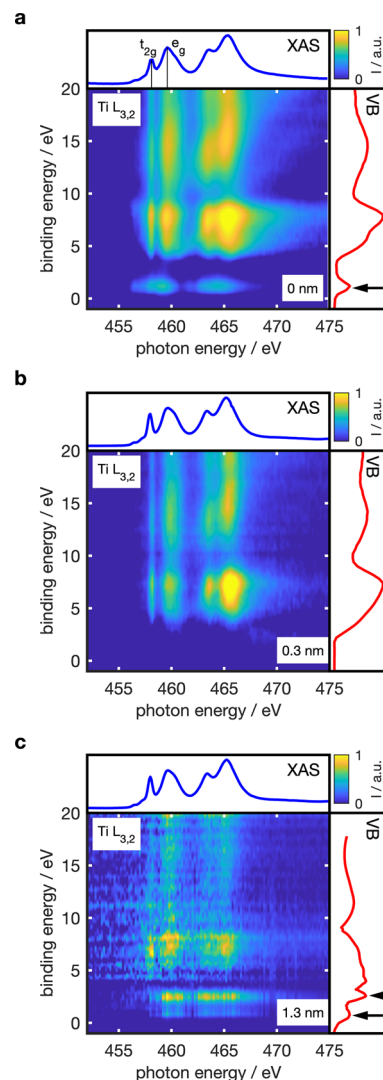


Figure 4. Resonant photoemission maps at the Ti L_{3,2} edge of (a) p⁺-Si/a-TiO₂, (b) p⁺-Si/a-TiO₂/Ni (0.3 nm), and (c) p⁺-Si/a-TiO₂/Ni (1.3 nm). The inset on the top shows the TEY-mode XAS spectrum. For (a), the positions of the t_{2g} and e_g bands at the Ti L₃ edge are indicated. The inset on the right shows the VB spectrum at 464 eV. In all spectra, the off-resonant contributions were subtracted using the off-resonant VB spectra at 452 eV scaled for photon flux. The black arrows on the right panel indicate the position of the gap state. The IMFP of VB electrons in TiO₂ for an excitation energy of 464 eV is 1.2 nm and was calculated using IMFP-TPP2M.⁴⁸ The IMFP gives an approximation of the PES sampling depth.

respectively.^{49,50} As the Ni thickness increased, the VBM shifted toward the Fermi energy.

Oxygen vacancies in a-TiO₂ result in n-type doping.²⁵ The localization of the extra electrons on Ti partially populates the t_{2g} band, this gives rise to the XPS peak observed at 1 eV BE in the a-TiO₂ band gap. In RiXS, this behavior is observed during resonant excitation from core levels into the e_g conduction band followed by de-excitation from the t_{2g} band, collectively producing a d–d loss feature.³³ Considering a t_{2g} gap state BE of 1 eV, a VBM of 2.94 eV BE, and a band gap of a-TiO₂ of 3.34 eV,⁶ the d–d transition is calculated to be >1.4 eV (i.e., the energy difference between the t_{2g} state (gap state) and the e_g state (CB minima, CBM)). The predicted d–d loss feature is shown in the RiXS spectra (Figure S7). The energy

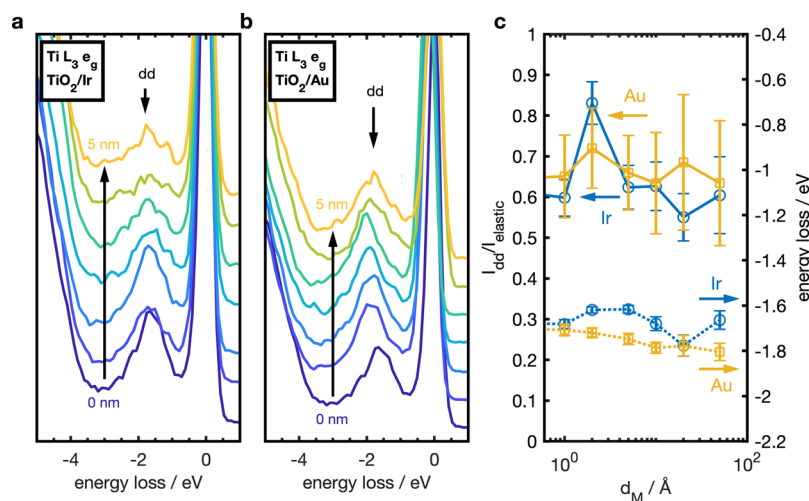


Figure 5. RIXS data of a-TiO₂/Ir (a) and a-TiO₂/Au (b) at the Ti L₃ e_g resonance. The position of the characteristic d–d transition is indicated. (c) Intensity ratio of the d–d transition to the elastic peak. A change in this normalized d–d intensity provides evidence about changes in the gap state.

difference between the t_{2g} and e_g bands can also be extracted from the TiO₂ XAS data. Figure 4a shows these data, indicating an energy difference of 1.6 eV. Both the TEY XAS and the constant initial state (CIS) XAS spectra of the gap state (0–3 eV BE, Figure S11) provide further evidence for the presence of these states and the gap state.

To illustrate the correlation between the VB gap state (XPS) and the d–d loss feature in RIXS, both measurements were performed on samples that did, and did not, respectively, have a gap state. Figure S7 shows the VB and RIXS data for pristine and then for annealed TDMAT a-TiO₂. For pristine a-TiO₂, the gap state is visible in the XPS VB, and the d–d transition peak is observed in the RIXS spectrum. Upon annealing, however, the gap state disappeared in the XPS data and no d–d transition was visible in RIXS.

As the X-ray attenuation length is much longer than the IMFP for electrons, a-TiO₂/M samples with increased metal thickness were prepared for RIXS measurements on a-TiO₂/Ir and a-TiO₂/Au. For a-TiO₂/Ir and a-TiO₂/Au interfaces (Figure 5a,b), the gap state was visible in the RIXS data as a characteristic d–d transition with an energy loss of 1.6 to 1.8 eV, with the elastic X-ray scattering peak at 0 eV. To obtain a signal that is directly proportional to the intensity of the gap state, the intensity of the d–d transition must be normalized to that of the elastic peak. Figure 5c shows the normalized gap state intensity and position as a function of metal coverage for both Ir and Au contacts. No clear change was evident as the coverage of the metal increased, suggesting that the gap state is unaffected by the deposition of Ir or Au.

4. DISCUSSION

4.1. Spectroscopic Characterization of Gap States.

Defect states in the band gap are well known for both crystalline and amorphous samples of TiO₂. Moreover, the interactions of metals and metal oxides with crystalline TiO₂ have been extensively investigated.²⁵ We have studied the interactions between Ni, Ir, and Au on amorphous a-TiO₂ grown at low temperatures by ALD. The use of a-TiO₂ to protect semiconductor photoelectrodes in PEC devices is an important aspect of the development of robust photoelectrodes that can split water. Previous experimental and theoretical

studies have implicated band gap states in a-TiO₂ for the conduction process.

ResPES allows the VB density of states for a p⁺ Si/a TiO₂/Ni electrode to be resolved into the partial density of states (pDOSs) of Ti, Ni, and O. Figure 6 shows the results for the a-

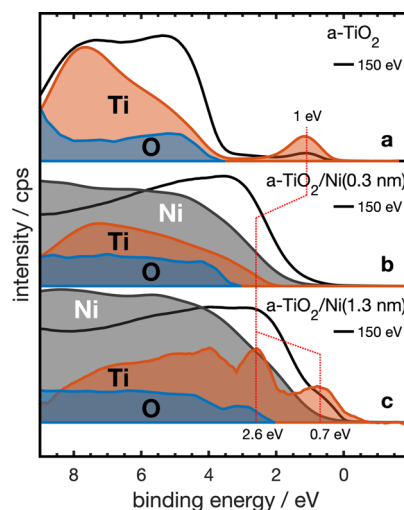


Figure 6. Partial density of VB states derived from titanium (red), oxygen (blue), and nickel (gray), respectively, at the a-TiO₂/Ni interface for pristine (a) a-TiO₂, (b) a-TiO₂/Ni(0.3 nm), and (c) a-TiO₂/Ni(1.3 nm). The pDOSs are obtained by calculating the difference between on- and off-resonance VB spectra at the Ti 2p, O 1s, and Ni 2p X-ray absorption edges. VB spectra recorded at a photon energy of 150 eV are included as a solid black curve (Figure S8).

TiO₂/Ni interface with varying thicknesses of Ni. Pristine TDMAT a-TiO₂ shows a titanium-derived gap state at 1 eV (Figure 6a). No change in the peak intensity was observed between the bulk and surface-sensitive XPS measurements for the gap state of pristine a-TiO₂ (Figure S6c). The gap state is observed by RIXS, which probes deeper into TiO₂ than XPS (Figures S7,S11), indicating that the state likely extends throughout the bulk of a-TiO₂ to the surface. Furthermore, previous studies have shown that hole conduction occurs by a

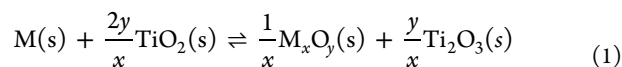
hopping mechanism (polaron transfer) in TiO₂ that uses Ti^{3+/4+} sites and requires that the gap state extend throughout the bulk.⁹

The resPES data showed that the gap state was not present at the a-TiO₂/Ni interface after deposition of a completely oxidized ultrathin Ni layer (0.3 nm) (Figures 6b, 2a and Figure S8b). Oxidation of ultrathin Ni layers by atmospheric water and oxygen is expected, and XPS data of an ultrathin Ni layer showed only NiO_x and no Ni metal (Figure S8b). After oxidation, NiO_x can donate oxygen species to TiO₂ and oxidize the interstitial surface Ti³⁺ sites. This process would create a thin interfacial layer with no Ti³⁺ gap states.^{26,27} Any reduced NiO_{x-y} would be reoxidized by ambient atmospheric O₂ and H₂O. A previous study has shown that interstitial Ti³⁺ sites can be healed by exposing the surface to an atmosphere of pure O₂.²⁷

4.2. Interfacial Reactivity Responsible for Gap States.

The work-function of NiO_x ($\Phi = 6.7$ eV) is substantially larger than that of metallic Ni.^{51,46} Although Φ may decrease upon exposure to H₂O, O₂, and/or CO₂, the value of Φ for Ni contacts should be larger than Φ for a-TiO₂ ($\Phi = 4.7$ eV). A high work-function material in contact with a-TiO₂ would reduce the charge-carrier population of a-TiO₂ near the interface by forcing electrons into the high work-function material to produce band bending in TiO₂. The loss of excess electrons reduces the number of Ti³⁺ states, which would decrease the number of conduction pathways and the rate of hole transfer, as shown in Figure S12b.^{9,52,45} The bulk properties of a-TiO₂ would not be affected by the loss of Ti³⁺ surface sites. This expectation is consistent with NiO_x donating oxygen atoms to a-TiO₂. In contrast to the results for Ni, thin layers of Au or Ir on a-TiO₂ showed no change in the intensity of the gap state (Figure 5).

A metal deposited on TiO₂ under vacuum can react as described in eq 1



The thermodynamics of the reaction are controlled by the standard heats of formation (ΔH_f) because the entropies of formation of the oxides are small.^{53,25} In general, early transition metals have more negative heats of formation than late transition metals. The ΔH_f value increases in the order Cr < Co < Ni, with the reaction of Cr to form Cr₂O₃ or Cr₃O₄ being slightly favorable thermodynamically.⁵⁴ Deposition of Cr under vacuum conditions onto rutile TiO₂ results in the reduction of TiO₂ at the surface and oxidation of the Cr metal, with the appearance of states within the TiO₂ band gap.¹⁹

However, in the work described herein, the very thin Ni layers (e.g., 0.3 nm) were fully oxidized in air. In this case, only NiO_x, as opposed to Ni metal, exists at the interface. The reaction is between reduced TiO₂ and NiO_x, resulting in eq 1 shifting to the left and the oxidation of reduced Ti at the interface. This results in the loss of the gap state at the interface for the 0.3 nm Ni sample.

For Ni thickness >0.3 nm, Ni at the a-TiO₂ interface was metallic. The XPS depth profiling revealed the presence of the metallic Ni phase under the electrochemically stable NiO_x surface layer (Figure S8).⁴⁵ In this case, resPES showed two gap states at the a-TiO₂/Ni interface, with binding energies of 0.7 and 2.6 eV (Figure 6c). The two states effectively filled the energy range between the VBM and the Fermi level. This

behavior was observed only for the a-TiO₂/Ni interface, whereas the bulk of a-TiO₂ was unaffected.

For the thick Ni layer (1.3 nm), the external NiO_x surface protected the underlying bulk metallic phase.⁴⁵ NiO_x was not initially present at the a-TiO₂ interface, excluding oxidation of Ti³⁺ (or Ti³⁺ interstitials). Oxidation of interfacial Ni would require Ni to capture oxygens from TiO₂, creating additional oxygen vacancies in a-TiO₂. Interfacial NiO_x could not be identified by XPS due to the presence of NiO_x on the outer surface. However, reduction of TiO₂ by the Ni metal would yield interfacial NiO_x, consistent with the ability of the neighboring elements Co and Fe to partially reduce TiO₂ and form a Co or Fe oxide.^{55,19} This behavior suggests that there are likely to be Ti–O–Ni interactions in the interfacial region.

The observation of two gap states agrees with earlier studies in which Cr and Co were deposited on rutile TiO₂ and analyzed in ultrahigh vacuum.¹⁹ For thin films of Co or Cr on TiO₂, resonant X-ray spectroscopy revealed gap states at 1.0 and 2.6 eV, with the higher-energy gap state assigned to the pDOS of Cr or Co.¹⁹ Figure 6 shows the presence of both gap states in the pDOS of Ti for thicker films of Ni on a-TiO₂, and shows a single gap state for bare a-TiO₂. These observations suggest that the gap state at 2.6 eV arises from an interaction between Ti and Ni (hybridization of Ti with Ni). A close inspection of the published Ti 2p resonant excitation VB spectra for TiO₂/Cr and TiO₂/Co (see Figures 5 and 10 in ref¹⁹) shows a small enhancement for Ti at 2.6 eV as well as a larger enhancement for Co 2p or Cr 2p resonant excitation.¹⁹ The resonant Ni spectra for a-TiO₂/Ni (1.3 nm) (Figure 6c and Figure S10b) show increased resonant Ni emission at 2.6 eV compared to a-TiO₂/Ni (0.3 nm). The increased Ni photoemission intensity indicates that Ni also contributes to the 2.6 eV feature.

The 2.6 eV feature observed in the VB Ti 2p edge (and its pDOS) is aligned with an increase in the pDOS of oxygen in the a-TiO₂/Ni (1.3 nm) sample, as shown in Figure 6c. The oxygen XAS has contributions from oxygens in both NiO_x and TiO₂, whereas the appearance of the peak in both the Ti and O pDOSs suggests that the feature is due to an interaction between Ti and Ni via an oxygen bridge, Ti–O–Ni.

The low-energy gap state (0.7 eV) indicates partial reduction of the a-TiO₂ surface by Ni⁰. The shift in BE from 1 to 0.7 eV for no Ni and 1.3 nm of Ni, respectively, is ascribed to the changes in the Ti³⁺ density and/or local symmetry (Ti moved from an octahedral position to a tetrahedral position at the interface).^{27,22} The density of gap states at the a-TiO₂/Ni (1.3 nm) interface between the VBM and the Fermi level energies produces a quasi-metallic interface that enhances conduction across this interface. Additional evidence for the existence of a quasi-metallic interface can be obtained by monitoring the edge position of the CIS XAS for states close to the Fermi energy (0–3 eV). The spectra are shown in Figure S11. The CIS spectrum of a-TiO₂/Ni (1.3 nm) shows an additional intensity at lower photon energies (<457 eV), which may suggest some reduction of TiO₂.^{56,57}

For the a-TiO₂/Ir and a-TiO₂/Au systems, only a single low-energy gap state was observed and the spectroscopy signal associated with this state did not change after metal deposition.

4.3. Protection Layer—Catalyst Band Alignment. At a semiconductor and metal junction, thermodynamics require equilibration of the electrochemical potentials by delocalized charge exchange. This charge exchange results in band bending and/or an interfacial dipole, δ , that shifts the potential between

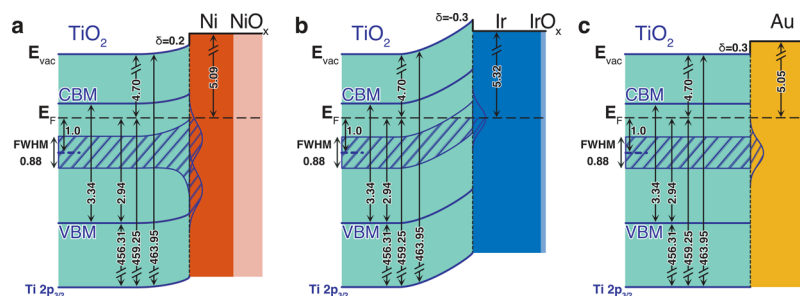


Figure 7. Band energy diagrams for a-TiO₂/M (5 nm) with M = nickel (a), M = iridium (b), and M = gold (c). All numeric values are in eV. δ is the interface dipole energy difference between TDMAT a-TiO₂ and the metal. The hashed region between the VBM and CBM in a-TiO₂ indicates the position of the gap state with the FWHM taken as its width. The values are also listed in Table S1. Gaussian peaks of the a-TiO₂/M interface illustrate the peak profile of the defect band.

the semiconductor bulk and the metal by the difference in the unequilibrated electrochemical potentials. The energy band profile relationships at a junction can be determined from XPS core-level and VB spectroscopy measurements in conjunction with UPS work-function measurements.⁵⁸ Because of the relatively small sampling depth of XPS, our approach involved measurement of differences between the VBM and core-level BE^{59,60} in conjunction with monitoring the variations of the well-defined core-level BE positions during step-by-step deposition of the metal with thicknesses between 5 and 30 Å.^{58,60} However, changes in the oxidation state, interfacial reactions, and lateral inhomogeneities have to be taken into account. The trend in the change of the Ti 2p_{3/2} core-level BE as a function of metal thickness is shown in Figure 3b. These changes in core-level BE reflect changes in band bending in a-TiO₂ close to the Ni interface as shown in Figure 7. Additional values extracted from XPS and UPS measurements (Figures 2 and 3) and from resPES (Figures 4,5) are collectively listed in Table S1.

Figure 7a–c shows the band profiles for a-TiO₂/M with M = Ni, Ir, or Au, as calculated by methods described previously.¹⁰ Both a-TiO₂/Ni and a-TiO₂/Ir have upward band bending at the interface, whereas a-TiO₂/Au has negligible band bending. In all three cases, the a-TiO₂ gap state is an intrinsic property of a-TiO₂ and thus extends throughout a-TiO₂. A previous study revealed that for thick Ni layers in a-TiO₂/Ni devices, the band bending in a-TiO₂ at the interface is fixed and independent of the applied potential in the electrolyte.⁴⁵ At the interface, the gap state fills the energy space between the VBM and Fermi level (Figure 7a). For thin layers, Ni was completely oxidized, and no interfacial gap state was detected (Figure 6b), which results in a thin interfacial layer that blocks the transport of holes from a-TiO₂ to the nickel catalyst. This behavior agrees with the lack of conduction observed in dc conductivity measurements of a-TiO₂/NiO_x contacts (Figure S2a, up to 0.7 nm).

For the a-TiO₂/Ir contact, only one gap state was detected at the interface, with a surface dipole that increased the band bending in a-TiO₂. The increased band bending causes the Fermi energy to pass through the top half of the gap state at the interface and results in an a-TiO₂ layer with a reduced Ti³⁺ concentration at the Ir interface (see also Figure S12). Since, charge transport is governed by a hopping mechanism, the rate is a function of the product of the concentrations of Ti⁴⁺ and Ti³⁺. Consequently, a reduction in Ti³⁺ sites produces a decrease in the conduction current. The lack of a quasi-metallic channel, and the low charge carrier density, is

consistent with the observed low conductivity of a-TiO₂/Ir contacts.

The a-TiO₂/Au interface showed no change in BE of the Ti 2p core levels and thus no upward band bending. The flat-band condition results in a lack of an electric field in TiO₂ that can propel holes toward the Au interface. This behavior is consistent with the observed low conductance of the a-TiO₂/Au system compared to the other two contacts. In addition, the a-TiO₂/Au system only conducted holes to the electrolyte for Au layers ≥ 10 nm in thickness. Thin layers of gold (≤ 5 nm) instead consisted of individual nanoparticles and showed negligible current (Figure S2).

4.4. Mixed Surface Barrier. In the a-TiO₂/Au nanoparticle system, a-TiO₂ contacts both the electrolyte and the Au nanoparticles and consequently produces nonuniform barrier heights (“pinch-off”) under an applied bias.⁶¹ Figure S4b shows the calculated potential inside TiO₂ for a 20 nm gold particle on the surface of a-TiO₂ under +1 V bias with periodic boundary conditions, with the respective band alignment shown in Figure S4c. The observations indicate upward bending in a-TiO₂ under the bulk electrolyte and downward band bending in a-TiO₂ under the Au nanoparticle. This behavior indicates an additional barrier for hole transport from a-TiO₂ to the metal nanoparticle, with the observed current dictated by the energetics of the a-TiO₂/electrolyte junction.

Previous studies have indicated that a shift in the applied bias at a-TiO₂/electrolyte systems is compensated by band bending in a-TiO₂ close to the electrolyte interface. Thus, a positive bias applied to a-TiO₂ will move the Fermi level below the bottom of the a-TiO₂ gap state (Figure S12a).^{45,52} This behavior results in depopulation of the gap state at the interface and formation of a thin depletion region with no Ti³⁺ sites, thus blocking hole transport. Consistently, no interfacial current was observed under these conditions.

5. CONCLUSIONS

The conduction behavior between “leaky” a-TiO₂ photoanode protection layers and metal catalysts (Ir, Ni, and Au) has been investigated in detail. Work-function differences between a-TiO₂ and the metal provide a guideline for band alignment at the a-TiO₂/M interface.⁹ A metal with a work-function less than that of a-TiO₂ generally exhibits high interfacial conductivity. However, the reactivity of the metal, its ability to oxidize or reduce interfacial a-TiO₂, and/or the ability to hybridize with Ti can affect the interfacial conductivity. Resonant X-ray spectroscopy revealed a critical interaction

between a-TiO₂ and Ni. For deposited Ni thickness of 0.3 nm, exposure to air fully oxidizes the Ni metal to NiO_x. The NiO_x can in turn oxidize the Ti³⁺ hopping sites in a-TiO₂ that block the transfer of holes to the Ni catalysts. Alternatively, Ni thickness of ≥1.3 nm protects Ni at the a-TiO₂ interface from oxidation and prevents oxidation of the Ti³⁺ hopping sites. The bands in a-TiO₂ are bent upward at the surface, which pushes holes toward the Ni interface. Furthermore, interactions between a-TiO₂ and Ni induce the formation of a second gap state in a-TiO₂ at the Ni contact. The band bending pushes holes through the a-TiO₂ layer, while the increased gap state density at the interface of the Ni catalyst provides a quasi-metallic ohmic contact between the phases. These changes result in the high conduction observed in the a-TiO₂/Ni system.

For the a-TiO₂/Ir system, the dipole at the surface increases the amount of band bending to the extent that the gap state is partially depleted. This reduces the conductivity through a-TiO₂, that together with the single gap state at the catalyst surface decreases the charge carrying capacity of the system. Furthermore, nonreactive metals that form nanoparticles, for example, Au, can lead to complete loss of catalytic current due to “pinch-off” effects that form a barrier for holes under anodic conditions.

The data suggest that the three characteristics of a highly conductive interface between a-TiO₂ and a metal contact are: (1) a “reductive” layer that does not oxidize the “leaky” a-TiO₂; (2) upward band bending that pushes holes toward the surface but does not push the Fermi level below the defect band in a-TiO₂; and (3) an increase in the a-TiO₂ density of states to provide a quasi-metallic interface with the metal.

■ ASSOCIATED CONTENT

Supporting Information

The Supporting Information is available free of charge at <https://pubs.acs.org/doi/10.1021/acs.chemmater.0c04043>.

Details on resonant photoemission measurements and supporting figures and tables (PDF)

■ AUTHOR INFORMATION

Corresponding Authors

Nathan S. Lewis – Division of Chemistry and Chemical Engineering, California Institute of Technology, Pasadena, California 91125, United States; Kavli Nanoscience Institute, California Institute of Technology, Pasadena, California 91125, United States; Beckman Institute, California Institute of Technology, Pasadena, California 91125, United States; orcid.org/0000-0001-5245-0538; Email: nslewis@caltech.edu

Bruce S. Brunschwig – Beckman Institute, California Institute of Technology, Pasadena, California 91125, United States; orcid.org/0000-0002-6135-6727; Email: bsb@caltech.edu

Authors

Matthias H. Richter – Division of Chemistry and Chemical Engineering, California Institute of Technology, Pasadena, California 91125, United States; orcid.org/0000-0003-0091-2045

Wen-Hui Cheng – Department of Applied Physics and Material Science, California Institute of Technology,

Pasadena, California 91125, United States; orcid.org/0000-0003-3233-4606

Ethan J. Crumlin – Advanced Light Source, Lawrence Berkeley National Laboratory, Berkeley, California 94720, United States; Chemical Sciences Division, Lawrence Berkeley National Laboratory, Berkeley, California 94720, United States; orcid.org/0000-0003-3132-190X

Walter S. Drisdell – Chemical Sciences Division, Lawrence Berkeley National Laboratory, Berkeley, California 94720, United States; orcid.org/0000-0002-8693-4562

Harry A. Atwater – Department of Applied Physics and Material Science, California Institute of Technology, Pasadena, California 91125, United States; Kavli Nanoscience Institute, California Institute of Technology, Pasadena, California 91125, United States; orcid.org/0000-0001-9435-0201

Dieter Schmeißer – BTU Cottbus, Applied Physics, Cottbus 03046, Germany

Complete contact information is available at: <https://pubs.acs.org/doi/10.1021/acs.chemmater.0c04043>

Author Contributions

[‡]M.H.R. and W.H.C. contributed equally to this work.

Notes

The authors declare no competing financial interest.

■ ACKNOWLEDGMENTS

This work was supported through the Office of Science of the U.S. Department of Energy (DOE) under award no. DE SC0004993 to the Joint Center for Artificial Photosynthesis, a DOE Energy Innovation Hub. Research was in part carried out at the Molecular Materials Research Center of the Beckman Institute of the California Institute of Technology. The Advanced Light Source is supported by the Director, Office of Science, Office of Basic Energy Sciences, of the U.S. Department of Energy under Contract No. DE AC02 05CH11231. E.J.C. was partially supported by an Early Career Award in the Condensed Phase and Interfacial Molecular Science Program in the Chemical Sciences, Geosciences, and Biosciences Division of the Office of Basic Energy Sciences of the U.S. Department of Energy under Contract No. DE-AC02-05CH11231. M.H.R. and W.H.C. carried out the investigation; E.J.C., W.S.D., H.A.A., and D.S. provided support for synchrotron studies and general discussion. M.H.R., W.H.C., N.S.L., and B.S.B. wrote the manuscript; and N.S.L. and B.S.B. supervised the study.

■ REFERENCES

- (1) Fountaine, K. T.; Lewerenz, H. J.; Atwater, H. A. Efficiency Limits for Photoelectrochemical Water-Splitting. *Nat. Commun.* **2016**, *7*, No. 13706.
- (2) Cheng, W.-H.; Richter, M. H.; May, M. M.; Ohlmann, J.; Lackner, D.; Dimroth, F.; Hannappel, T.; Atwater, H. A.; Lewerenz, H.-J. Monolithic Photoelectrochemical Device for Direct Water Splitting With 19% Efficiency. *ACS Energy Lett.* **2018**, *3*, 1795–1800.
- (3) Fountaine, K. T.; Lewerenz, H. J. Efficiency Limits for Hydrogen and Formate Production via Fully-Integrated Photoelectrochemical Devices. *ECS Trans.* **2017**, *77*, 15–23.
- (4) May, M. M.; Lackner, D.; Ohlmann, J.; Dimroth, F.; van de Krol, R.; Hannappel, T.; Schwarzburg, K. On the benchmarking of multi-junction photoelectrochemical fuel generating devices. *Sustainable Energy Fuels* **2017**, *1*, 492–503.

- (5) Cheng, W.-H.; Richter, M. H.; Sullivan, I.; Larson, D. M.; Xiang, C.; Brunschwig, B. S.; Atwater, H. A. CO₂ Reduction to CO With 19% Efficiency in a Solar-Driven Gas Diffusion Electrode Flow Cell Under Outdoor Solar Illumination. *ACS Energy Lett.* **2020**, *5*, 470–476.
- (6) Hu, S.; Shaner, M. R.; Beardslee, J. A.; Lichterman, M.; Brunschwig, B. S.; Lewis, N. S. Amorphous TiO₂ coatings stabilize Si, GaAs, and GaP photoanodes for efficient water oxidation. *Science* **2014**, *344*, 1005–1009.
- (7) Sun, K.; Saadi, F. H.; Lichterman, M. F.; Hale, W. G.; Wang, H.-P.; Zhou, X.; Plymale, N. T.; Omelchenko, S. T.; He, J.-H.; Papadantonakis, K. M.; Brunschwig, B. S.; Lewis, N. S. Stable solar-driven oxidation of water by semiconducting photoanodes protected by transparent catalytic nickel oxide films. *Proc. Natl. Acad. Sci.* **2015**, *112*, 3612–3617.
- (8) Bae, D.; Seger, B.; Vesborg, P. C. K.; Hansen, O.; Chorkendorff, I. Strategies for Stable Water Splitting via Protected Photoelectrodes. *Chem. Soc. Rev.* **2017**, *46*, 1933–1954.
- (9) Nunez, P.; Richter, M. H.; Piercy, B. D.; Roske, W. C.; Cabañ-Acevedo, M.; Losego, M. D.; Konezny, S. J.; Fermin, D. J.; Hu, S.; Brunschwig, B. S.; Lewis, N. S. Characterization of Electronic Transport through Amorphous TiO₂ Produced by Atomic Layer Deposition. *J. Phys. Chem. C* **2019**, *123*, 20116–20129.
- (10) Hu, S.; Richter, M. H.; Lichterman, M. F.; Beardslee, J.; Mayer, T.; Brunschwig, B. S.; Lewis, N. S. Electrical, Photoelectrochemical, and Photoelectron Spectroscopic Investigation of the Interfacial Transport and Energetics of Amorphous TiO₂/Si Heterojunctions. *J. Phys. Chem. C* **2016**, *120*, 3117–3129.
- (11) Sze, S. M.; Ng, K. N. *Physics of Semiconductor Devices*. Wiley Interscience: New York, 2006; 134–191.
- (12) McCrory, C. C. L.; Jung, S.; Ferrer, I. M.; Chatman, S. M.; Peters, J. C.; Jaramillo, T. F. Benchmarking Hydrogen Evolving Reaction and Oxygen Evolving Reaction Electrocatalysts for Solar Water Splitting Devices. *J. Am. Chem. Soc.* **2015**, *137*, 4347–4357.
- (13) Chen, G.; Zhou, W.; Guan, D.; Sunarso, J.; Zhu, Y.; Hu, X.; Zhang, W.; Shao, Z. Two Orders of Magnitude Enhancement in Oxygen Evolution Reactivity on Amorphous Ba_{0.5}Sr_{0.5}Co_{0.8}Fe_{0.2}O_{3-δ} Nanofilms With Tunable Oxidation State. *Sci. Adv.* **2017**, *3*, No. e1603206.
- (14) Hufnagel, A. G.; Henß, A.; Hoffmann, R.; Zeman, O. E. O.; Häringer, S.; Fattakhova-Rohlfing, D.; Bein, T. Electron-Blocking and Oxygen Evolution Catalyst Layers by Plasma-Enhanced Atomic Layer Deposition of Nickel Oxide. *Adv. Mater. Interfaces* **2018**, *5*, No. 1701531.
- (15) Patel, M.; Kim, J. Thickness-Dependent Photoelectrochemical Properties of a Semitransparent Co₃O₄ Photocathode. *Beilstein J. Nanotechnol.* **2018**, *9*, 2432–2442.
- (16) Zhou, X.; Liu, R.; Ke, S.; Papadantonakis, K. M.; Brunschwig, B. S.; Lewis, N. S. 570 mV Photovoltage, Stabilized N-Si/CoOx Heterojunction Photoanodes Fabricated Using Atomic Layer Deposition. *Energy Environ. Sci.* **2016**, *9*, 892–897.
- (17) Lichterman, M. F.; Sun, K.; Shu, H.; Zhou, X.; McDowell, M. T.; Shaner, M. R.; Richter, M. H.; Crumlin, E. J.; Carim, A. I.; Saadi, F. H.; Brunschwig, B. S.; Lewis, N. S. Protection of Inorganic Semiconductors for Sustained, Efficient Photoelectrochemical Water Oxidation. *Catal. Today* **2016**, *262*, 11–23.
- (18) Morales, F.; de Groot, F. M. F.; Glatzel, P.; Kleimenov, E.; Bluhm, H.; Hävecker, M.; Knop-Gericke, A.; Weckhuysen, B. M. In Situ X-ray Absorption of Co/Mn/TiO₂ Catalysts for Fischer–Tropsch Synthesis. *J. Phys. Chem. B* **2004**, *108*, 16201–16207.
- (19) Müller, S.; Schmeißer, D. *Deposition of reactive and non-reactive metals on titanium dioxide - Chromium and cobalt*. 2008 International Students and Young Scientists Workshop - Photonics and Microsystems 2008, 53–58.
- (20) Nagatsuka, N.; Wilde, M.; Fukutani, K. Hydrogenation and hydrogen diffusion at the anatase TiO₂(101) surface. *J. Chem. Phys.* **2020**, *152*, No. 074708.
- (21) Ohashi, Y.; Nagatsuka, N.; Ogura, S.; Fukutani, K. Hydrogen Distribution and Electronic Structure of TiO₂(110) Hydrogenated with Low-Energy Hydrogen Ions. *J. Phys. Chem. C* **2019**, *123*, 10319–10324.
- (22) Di Valentin, C.; Pacchioni, G.; Selloni, A. Reduced and n-Type Doped TiO₂: Nature of Ti³⁺ Species. *J. Phys. Chem. C* **2009**, *113*, 20543–20552.
- (23) Krischok, S.; Günster, J.; Goodman, D. W.; Höfft, O.; Kempter, V. MIES and UPS(HeI) studies on reduced TiO₂(110). *Surf. Interface Anal.* **2005**, *37*, 77–82.
- (24) Li, M.; Song, W.; Zeng, L.; Zeng, D.; Xie, C.; Yang, Q. Mechanistic study of N–H- and H–N-codoping of a TiO₂ photocatalyst for efficient degradation of benzene under visible light. *RSC Adv.* **2020**, *10*, 2757–2766.
- (25) Diebold, U. The Surface Science of Titanium Dioxide. *Surf. Sci. Rep.* **2003**, *48*, 53–229.
- (26) Henderson, M. A. A Surface Perspective on Self-Diffusion in Rutile TiO₂. *Surf. Sci.* **1999**, *419*, 174–187.
- (27) Wendt, S.; Sprunger, P. T.; Lira, E.; Madsen, G. K. H.; Li, Z.; Hansen, J. Ø.; Matthiesen, J.; Blekinge-Rasmussen, A.; Lægsgaard, E.; Hammer, B.; Besenbacher, F. The Role of Interstitial Sites in the Ti3d Defect State in the Band Gap of Titania. *Science* **2008**, *320*, 1755–1759.
- (28) Reckers, P.; Dimamay, M.; Klett, J.; Trost, S.; Zilberberg, K.; Riedl, T.; Parkinson, B. A.; Brötz, J.; Jaegermann, W.; Mayer, T. Deep and Shallow TiO₂ Gap States on Cleaved Anatase Single Crystal (101) Surfaces, Nanocrystalline Anatase Films, and ALD Titania Ante and Post Annealing. *J. Phys. Chem. C* **2015**, *119*, 9890–9898.
- (29) Mehta, M.; Kodan, N.; Kumar, S.; Kaushal, A.; Mayrhofer, L.; Walter, M.; Moseler, M.; Dey, A.; Krishnamurthy, S.; Basu, S.; Singh, A. P. Hydrogen treated anatase TiO₂: a new experimental approach and further insights from theory. *J. Mater. Chem. A* **2016**, *4*, 2670–2681.
- (30) Pham, H. H.; Wang, L.-W. Oxygen vacancy and hole conduction in amorphous TiO₂. *Phys. Chem. Chem. Phys.* **2015**, *17*, 541–550.
- (31) Henkel, K.; Kot, M.; Richter, M. H.; Tallarida, M.; Schmeißer, D. An (In Situ)² Approach: ALD and resPES Applied to Al₂O₃, HfO₂, and TiO₂ Ultrathin Films. In *Encyclopedia of Interfacial Chemistry: Surface Science and Electrochemistry*; Wandelt, K., Ed.; Elsevier, 2018; 3.1, 18–26.
- (32) Das, C.; Richter, M. H.; Tallarida, M.; Schmeißer, D. Electronic Properties of Atomic Layer Deposition Films, Anatase and Rutile TiO₂ Studied by Resonant Photoemission Spectroscopy. *J. Phys. D: Appl. Phys.* **2016**, *49*, No. 275304.
- (33) Moser, S.; Fatale, S.; Krüger, P.; Berger, H.; Bugnon, P.; Magrez, A.; Niwa, H.; Miyawaki, J.; Harada, Y.; Grioni, M. Electron-Phonon Coupling in the Bulk of Anatase TiO₂ Measured by Resonant Inelastic X-Ray Spectroscopy. *Phys. Rev. Lett.* **2015**, *115*, No. 096404.
- (34) Glatzel, P.; Sikora, M.; Fernandez-Garcia, M. Resonant X-Ray Spectroscopy to Study K Absorption Pre-Edges in 3D Transition Metal. *Eur. Phys. J. Spec. Top.* **2009**, *169*, 207–214.
- (35) Lichterman, M. F.; Carim, A. I.; McDowell, M. T.; Hu, S.; Gray, H. B.; Brunschwig, B. S.; Lewis, N. S. Stabilization of n-cadmium telluride photoanodes for water oxidation to O₂(g) in aqueous alkaline electrolytes using amorphous TiO₂ films formed by atomic-layer deposition. *Energy Environ. Sci.* **2014**, *7*, 3334–3337.
- (36) Lichterman, M. F.; Richter, M. H.; Hu, S.; Crumlin, E. J.; Axnanda, S.; Favaro, M.; Drisdell, W.; Hussain, Z.; Mayer, T.; Brunschwig, B. S.; Lewis, N. S.; Liu, Z.; Lewerenz, H. J. Investigation of the Si/TiO₂/Electrolyte Interface Using Operando Tender X-ray Photoelectron Spectroscopy. *ECS Trans.* **2015**, *66*, 97–103.
- (37) Richter, M. H.; Lichterman, M. F.; Hu, S.; Crumlin, E. J.; Mayer, T.; Axnanda, S.; Favaro, M.; Drisdell, W.; Hussain, Z.; Brunschwig, B. S.; Lewis, N. S.; Liu, Z.; Lewerenz, H. J. Measurement of the Energy-Band Relations of Stabilized Si Photoanodes Using Operando Ambient Pressure X-ray Photoelectron Spectroscopy. *ECS Trans.* **2015**, *66*, 105–113.
- (38) Schmeißer, D.; Hoffmann, P.; Beuckert, G. Electronic Properties of the Interface Formed by Pr₂O₃ Growth on Si(001), Si(111) and SiC(0001) Surfaces. In *Materials for Information*

Technology; Zschech, E., Whelan, C., Mikolajick, T., Eds.; Springer: London, 2005; 449–459, DOI: 10.1007/1-84628-235-7_36.

(39) Stöhr, J. *NEXAFS Spectroscopy*. Ertl, G., Gomer, R., Mills, D. L., Eds.; Springer: Heidelberg, 2003; 25, 154–161, 276–291.

(40) Grass, M. E.; Karlsson, P. G.; Aksoy; Lundqvist, M.; Wannberg, B.; Mun, B. S.; Hussain, Z.; Liu, Z. New Ambient Pressure Photoemission Endstation at Advanced Light Source Beamline 9.3.2. *Rev. Sci. Instrum.* **2010**, *81*, No. 053106.

(41) Qiao, R.; Li, Q.; Zhuo, Z.; Sallis, S.; Fuchs, O.; Blum, M.; Weinhardt, L.; Heske, C.; Pepper, J.; Jones, M.; Brown, A.; Spucce, A.; Chow, K.; Smith, B.; Glans, P.-A.; Chen, Y.; Yan, S.; Pan, F.; Pipper, L. F. J.; Denlinger, J.; Guo, J.; Hussain, Z.; Chung, Y.-D.; Yang, W. High-efficiency in situ resonant inelastic x-ray scattering (iRIXS) endstation at the Advanced Light Source. *Rev. Sci. Instrum.* **2017**, *88*, No. 033106.

(42) Friebel, D.; Louie, M. W.; Bajdich, M.; Sanwald, K. E.; Cai, Y.; Wise, A. M.; Cheng, M.-J.; Sokaras, D.; Weng, T.-C.; Alonso-Mori, R.; Davis, R. C.; Bargar, J. R.; Nørskov, J. K.; Nilsson, A.; Bell, A. T. Identification of Highly Active Fe Sites in (Ni, Fe)OOH for Electrocatalytic Water Splitting. *J. Am. Chem. Soc.* **2015**, *137*, 1305–1313.

(43) Michaelson, H. B. The work function of the elements and its periodicity. *J. Appl. Phys.* **1977**, *48*, 4729–4733.

(44) Hofmann, T.; Yu, T. H.; Folse, M.; Weinhardt, L.; Bär, M.; Zhang, Y.; Merinov, B. V.; Myers, D. J.; Goddard, W. A., III; Heske, C. Using Photoelectron Spectroscopy and Quantum Mechanics to Determine d-Band Energies of Metals for Catalytic Applications. *J. Phys. Chem. C* **2012**, *116*, 24016–24026.

(45) Lichterman, M. F.; Richter, M. H.; Hu, S.; Crumlin, E. J.; Axnanda, S.; Favaro, M.; Drisdell, W.; Hussain, Z.; Bruntschwig, B. S.; Lewis, N. S.; Liu, Z.; Lewerenz, H. J. An Electrochemical, Microtopographical and Ambient Pressure X-Ray Photoelectron Spectroscopic Investigation of Si/TiO₂/Ni/Electrolyte Interfaces. *J. Electrochem. Soc.* **2015**, *163*, H139–H146.

(46) Greiner, M. T.; Chai, L.; Helander, M. G.; Tang, W.-M.; Lu, Z.-H. Transition Metal Oxide Work Functions: The Influence of Cation Oxidation State and Oxygen Vacancies. *Adv. Funct. Mater.* **2012**, *22*, 4557–4568.

(47) Kashiwaya, S.; Morasch, J.; Streibel, V.; Toupance, T.; Jaegermann, W.; Klein, A. The Work Function of TiO₂. *Surfaces* **2018**, *1*, 73–89.

(48) Tanuma, S.; Powell, C. J.; Penn, D. R. Calculations of electron inelastic mean free paths. V. Data for 14 organic compounds over the 50–2000 eV range. *Surf. Interface Anal.* **1994**, *21*, 165–176.

(49) Cho, D.-Y.; Song, S. J.; Kim, U. K.; Kim, K. M.; Lee, H.-L.; Hwang, C. S. Spectroscopic Investigation of the Hole States in Ni-Deficient NiO Films. *J. Mater. Chem. C* **2013**, *1*, 4334–4338.

(50) Mossanek, R. J. O.; Dominguez-Canizares, G.; Gutierrez, A.; Abbate, M.; Diaz-Fernandez, D.; Soriano, L. Effects of Ni vacancies and crystallite size on the O 1s and Ni 2p x-ray absorption spectra of nanocrystalline NiO. *J. Phys.: Condens. Matter* **2013**, *25*, No. 495506.

(51) Greiner, M. T.; Helander, M. G.; Wang, T.-B.; Tang, W.-M.; Lu, Z.-H. Effects of Processing Conditions on the Work Function and Energy-Level Alignment of NiO Thin Films. *J. Phys. Chem. C* **2010**, *114*, 19777–19781.

(52) Lichterman, M. F.; Hu, S.; Richter, M. H.; Crumlin, E. J.; Axnanda, S.; Favaro, M.; Drisdell, W.; Hussain, Z.; Mayer, T.; Bruntschwig, B. S.; Lewis, N. S.; Liu, Z.; Lewerenz, H. J. Direct observation of the energetics at a semiconductor/liquid junction by operando X-ray photoelectron spectroscopy. *Energy Environ. Sci.* **2015**, *8*, 2409–2416.

(53) Campbell, C. T. Ultrathin Metal Films and Particles on Oxide Surfaces: Structural, Electronic and Chemisorptive Properties. *Surf. Sci. Rep.* **1997**, *27*, 1–111.

(54) *CRC Handbook of Chemistry and Physics*. Rumble, J. R., Ed.; CRC Press, 2017; 9: 64.

(55) Diebold, U.; Pan, J.-M.; Madey, T. E. Ultrathin Metal Film Growth on TiO₂(110): An Overview. *Surf. Sci.* **1995**, *331–333*, 845–854.

(56) Rotundu, C. R.; Jiang, S.; Deng, X.; Qian, Y.; Khan, S.; Hawthorn, D. G.; Kotliar, G.; Ni, N. Physical Properties and Electronic Structure of a New Barium Titanate Suboxide Ba_{1+δ}Ti_{13-δ}O₁₂ (δ = 0.11). *APL Mater.* **2015**, *3*, No. 041517.

(57) Singh, R.; Gupta, M.; Phase, D. M.; Mukherjee, S. K. Phase Growth Analysis of Sputtered TiO₂ Thin Films at Low Oxygen Partial Pressures Using XANES and XRR. *Mater. Res. Express* **2019**, *6*, 116449.

(58) Mankel, E.; Hein, C.; Kühn, M.; Mayer, T. Electric potential distributions in space charge regions of molecular organic adsorbates using a simplified distributed states model. *Phys. Status Solidi A* **2014**, *211*, 2040–2048.

(59) Horn, K. Semiconductor Interface Studies Using Core and Valence Level Photoemission. *Appl. Phys. A: Mater. Sci. Process.* **1990**, *51*, 289–304.

(60) Franciosi, A.; Van de Walle, C. G. Heterojunction Band Offset Engineering. *Surf. Sci. Rep.* **1996**, *25*, 1–140.

(61) Rossi, R. C.; Lewis, N. S. Investigation of the Size-Scaling Behavior of Spatially Nonuniform Barrier Height Contacts to Semiconductor Surfaces Using Ordered Nanometer-Scale Nickel Arrays on Silicon Electrodes. *J. Phys. Chem. B* **2001**, *105*, 12303–12318.